npj | climate and atmospheric science

Article

Published in partnership with CECCR at King Abdulaziz University

https://doi.org/10.1038/s41612-025-00934-z

Sulfate formation through copper-catalyzed SO_2 oxidation by NO_2 at aerosol surfaces

Pai Liu[1,3], Yu-Xin Liu[1,3], Qishen Huang[1] ✉, Xinyue Chao[1], Mingrui Zhong[1], Jiayi Yin[1], Xiaowu Zhang[1], Lin-Fang Li[1], Xi-Yuan Kang[1], Zhe Chen[1], Shufeng Pang[1], Weigang Wang[2], Yun-Hong Zhang[1] ✉ & Maofa Ge[2] ✉

Severe urban air pollution in China is driven by a synergistic conversion of SO_2, NOx, and NH_3 into fine particulate matter ($PM_{2.5}$). Field studies indicated NO_2 as an important oxidizer to SO_2 in polluted atmospheres with low photochemical reactivity, but this rapid reaction cannot be explained by the aqueous reactive nitrogen chemistry in acidic urban aerosols. Here, using an aerosol optical tweezer and Raman spectroscopy, we show that the multiphase SO_2 oxidation by NO_2 is accelerated for two-order-of-magnitude by a copper catalyst. This reaction occurs on aerosol surfaces, is independent of pH between 3 and 5, and produces sulfate by a rate of up to 10 μg m^{-3}_{air} hr^{-1} when reactive copper reaches a millimolar concentration in aerosol water – typical of severe haze events in North China Plain. Since copper and NO_2 are companion emitters in air pollution, they can act synergistically in converting SO_2 into sulfate in China's haze.

Air pollution is a persistent problem in developing countries, such as China and other emerging economies experiencing rapid industrialization[1–3]. Among the pollutants, the principal culprit is fine particulate matter ($PM_{2.5}$), the airborne particles that can penetrate into human lungs, leading to premature deaths from cardiovascular and respiratory diseases and lung cancer[4,5]. To mitigate $PM_{2.5}$ and its public health impacts, the Chinese government renewed its air-quality policies in 2021, aiming for a 10% reduction of urban $PM_{2.5}$ concentration by 2025[6]. Achieving this objective requires a clear understanding of the atmospheric chemistry producing $PM_{2.5}$ in urban haze.

China's haze differs from London fog or Los Angeles smog in several ways. First, gas pollutants coexist at high concentrations[3,7–9], including SO_2, NOx (NO and NO_2), and NH_3, emitted from industry, traffic, and agriculture[10–12]. These gases convert synergistically into $PM_{2.5}$ through atmospheric multiphase reactions[3,7–9]. Second, the multiphase reactions occur rapidly, much faster than what aqueous chemistry predicts[8,13–15]. Such rapid kinetics may result from many factors, including enhanced chemical reactivities at the air-water interface[14,16,17], the catalytic effects of transition metal ions (TMI)[13,18], or the salt effects in the oversaturated aerosol water[15,19] – or all these factors acting simultaneously. Recognizing these characteristics, scientists coined the term *haze chemistry* to describe how $PM_{2.5}$ is formed during the severe urban air pollution in China[3,7–9,20].

A decade-long debate in haze chemistry research concerns whether NO_2 can effectively oxidize SO_2 into sulfate, thereby contributing to $PM_{2.5}$ formation. Why is NO_2 considered an oxidizer of SO_2? First, this redox reaction can occur in the atmospheric environments; NO_2 can oxidize SO_2 on the surfaces of primary particles (i.e., soot[21] and dust[9]) and, more prevalently, in aerosol water[7,22–24]:

$$2NO_{2(aq)} + HSO^-_{3(aq)} + H_2O \rightarrow H^+_{(aq)} + 2HONO_{(aq)} + SO^{2-}_{4(aq)} \quad \text{(Reaction1)}$$

Additionally, NO_2 is abundant in the urban haze, especially when photochemical oxidizers such as O_3, H_2O_2, and OH are inhibited in the polluted troposphere dimmed by haze[8] or at night[25]. Field campaigns in China[8,26,27] showed that sulfate and NO_2 concentrations are positively correlated. A Beijing campaign[25] found that the HONO produced by Reaction 1 can even further oxidize SO_2. An air-quality model[8] predicted that, at pH 5.8, the reaction between HSO_3^- and NO_2 (hereafter, the HSO_3^-/NO_2 reaction, and so forth) would produce sulfate by a rate of 10 μg m^{-3}_{air} hr^{-1}. A laboratory study[14] found that, at pH 6, a SO_3^{2-}/NO_2 reaction would produce sulfate by 90 μg m^{-3}_{air} hr^{-1}.

[1]Institute of Chemical Physics, School of Chemistry and Chemical Engineering, Beijing Institute of Technology, Beijing, China. [2]State Key Laboratory for Structural Chemistry of Unstable and Stable Species, Beijing National Laboratory for Molecular Sciences, CAS Research/Education Center for Excellence in Molecular Sciences, Institute of Chemistry, Chinese Academy of Sciences, Beijing, China. [3]These authors contributed equally: Pai Liu, Yu-Xin Liu.
✉e-mail: qishenh@bit.edu.cn; yhz@bit.edu.cn; gemaofa@iccas.ac.cn

These studies suggested that sulfate $PM_{2.5}$ in China's haze was produced mainly through the NO_2 reaction pathway.

Yet equally compelling evidence indicates that NO_2 contributed to SO_2 oxidation negligibly. Although Reaction 1 can occur in the aqueous phase, it is unlikely to occur through a direct electron transfer, because the redox potentials between aqueous HSO_3^- and NO_2 are close[28,29]. The reaction instead occurs through the formation of $[NO_2\text{-}SO_3]^{2-}$ adducts, which decompose to SO_3^- radicals slowly[28]. This kinetic constraint rules out a rapid sulfate formation through Reaction 1. Additionally, the average pH of urban aerosols in China[30] is approximately 4, which is more acidic than what previous studies have assumed[8]. At acidic conditions, SO_2 has limited solubility, leaving too few S(IV) ions (HSO_3^- and SO_3^{2-}) to facilitate a rapid sulfate formation[13,31]. At pH 4, the sulfate formation rate via HSO_3^-/NO_2[8] and SO_3^{2-}/NO_2[14] reactions are respectively 0.04 and 0.15 $\mu g\, m^{-3}{}_{air}\, hr^{-1}$. Recent air-quality models[13,32] showed that the HSO_3^-/NO_2 reaction contributed approximately 0.1% of sulfate[13]; the SO_3^{2-}/NO_2 reaction, approximately 0.4%[32]. A source apportion study[31] showed that the NO_2 reaction pathway contributed at most 1% of sulfate in China haze. A recent global-scale study[33] found that the NO_2 reaction pathway is unimportant unless aerosol pH is above 5, a condition rarely met worldwide.

These disagreements[8,25–30,33] indicate a knowledge gap regarding how sulfate is produced in urban air pollution. Why does it matter whether NO_2 contributes to sulfate formation? If so, then both SO_2 and NO_2 would be sulfate precursors, and effective abatement would require closer coordination between the industry and transportation sectors[3,7–11]. Bridging this knowledge gap requires us to answer the following question: Can the multiphase SO_2 oxidation by NO_2 occur rapidly at acidic conditions?

Here, we show that NO_2 can oxidize SO_2 into sulfate rapidly at acidic conditions when the reaction is catalyzed by copper (hereafter, Cu). Cu, albeit a transition metal, is a weak catalyst for S(IV) oxidation by O_2[34]. But Cu is a strong catalyst for NO_2 reduction by S(IV) in flue gas de-nitrification[35,36]. Additionally, Cu is ubiquitous in urban air pollution[37]. A field campaign[38] reported that Cu elements were on the orders of hundreds of ng $m^{-3}{}_{air}$ during the air pollution in North China Plain (NCP). In Beijing, Cu mainly originates from traffic emissions, i.e., brake and tire wear[39]; in the broader NCP region, Cu mainly originates from coal combustions[39]. On the other hand, NO_2 originates from both industrial and traffic emissions[11,12], and its concentration can reach 40-to-80 ppb during heavy air pollution in NCP[8]. In other words, Cu and NO_2 are companion emitters, and they may synergistically convert SO_2 into sulfate during urban haze. Furthermore, we show that the kinetics of the ternary $Cu/SO_2/NO_2$ reaction depends more sensitively on NO_2 concentration, rather than on SO_2 concentration. This may explain why, over the past decade, a substantial decrease in SO_2 emission has not led to a proportional decrease in sulfate concentration in China.

Results

Method summary

We studied the Cu-catalyzed reaction with Raman micro-spectrometry (hereafter, micro-Raman) and an aerosol optical tweezer (hereafter, AOT). The micro-Raman experiments provided information on the reaction mechanism, including the reaction products, the catalytic effect of Cu(II) ions, and kinetic dependence on droplet size (radius 5–30 μm) and acidity (pH 3–5). The AOT experiments provided kinetic data for the reactions in levitated droplets, under conditions closely mimicking urban air pollutions, such as droplet solute ($(NH_4)_2SO_4$), acidity (pH 4), relative humidity (RH 60%), and reactant gases mixing ratio (SO_2, 5–200 ppb; NO_2, 50–500 ppb), and reaction time (hours). We designed these experiments based on literature values of aerosol pH[13,30], gas concentrations[8], and RH conditions[14]. Specifically, the ranges of these parameters encompass their average values during severe pollution events in Beijing (i.e., pH 4, SO_2 40 ppb, NO_2 66 ppb). Refer to the Methods section for details.

Copper-catalyzed SO_2 oxidation by NO_2

Figure 1A shows the Raman spectra of microdroplets, which served as reactors for the oxidation of SO_2 (500 ppb) by NO_2 (500 ppb). Droplet pH was buffered at approximately 4 with 400 ppb NH_3[40]. Ambient RH was approximately 80%. The left panel represents the reaction catalyzed by Cu(II) ions in the microdroplet seeded with a mixture of $NH_4Cl/HCl/CuCl_2$ (1:0.005:0.001). Here, the Raman spectrum exhibits a peak around 980 cm^{-1}, indicating SO_4^{2-} formation (See Figure S1 for the full spectrum). This catalyzed reaction produced approximately 0.4 M sulfate in 240 min. Contrastingly, the right panel represents the uncatalyzed reaction in the microdroplet seeded with NH_4Cl/HCl (1:0.005). This uncatalyzed reaction was too slow to be measured with the micro-Raman. In Figure S2, the AOT data shows that the reaction catalyzed by 0.1% Cu-in-solute was faster than the uncatalyzed reaction by two orders of magnitude. In both cases, the reaction did not produce NO_3^-, which would exhibit a Raman peak at 1050 cm^{-3}. In other words, NO_2 served only as an oxidizer of SO_2 and did not undergo disproportionation at our experimental conditions. Figure S3 shows another control experiment, where NO_2 was not applied, and no sulfate was produced within 240 min.

Figure 1B–D show the kinetic dependence on droplet size and acidity. These experiments were conducted in $NH_4Cl/HCl/CuCl_2$ droplets (1:0.005:0.001), with a radius (hereafter, a) between 5 and 30 μm. Other conditions were 500 ppb SO_2, 500 ppb NO_2, 40-to-4000 ppb NH_3, and 80% RH. Figure 1B shows that the reaction is faster in smaller droplets. Specifically, the SO_4^{2-} formation rate, $d\left[SO_4^{2-}\right]/dt$, (unit: M s^{-1}) is inversely proportional to droplet radius, a (See the dotted line in Fig.1C). This relationship indicates that the reaction rate is proportional to the droplet surface-area-to-volume ratio, such as A/V. Hereafter, we will normalize kinetic data as below:

$$R = \frac{Vd\left[SO_4^{2-}\right]}{Adt} \tag{1}$$

Here, R has a unit of mol s^{-1} μm^{-2} and it quantifies the reaction rate on a surface-area basis. Meanwhile, we also conducted experiments in the pH-resolved droplets, which were buffered at pH 3, 4, or 5 with 40, 400, or 4000 ppb NH_3, respectively. Figure 1B–D show that the reaction rate is unaffected by pH between 3 and 5. Figure S4 shows that the reaction remains unaffected by acidity in the unbuffered droplets, where the pH decreased to a level between 0 and 1 owing to the production of sulfuric acid, H_2SO_4. In summary, Cu can accelerate SO_2 oxidation by NO_2 by two orders of magnitude. The reaction rate scales with droplet surface area and is independent of pH. These observations indicate that SO_2 directly converts to sulfate at droplet surfaces.

Reaction mechanism

We propose the following mechanism for the Cu-catalyzed SO_2 oxidation by NO_2 on aerosol surfaces:

$$SO_2 \cdot H_2O + Cu(II) \xrightarrow{k_2} SO_3^- + Cu(I) + 2H^+ \quad \text{(Reaction2)}$$

$$NO_2 + Cu(I) \xrightarrow{k_3} NO_2^- + Cu(II) \quad \text{(Reaction3)}$$

$$SO_3^- + NO_2 \rightarrow NO_2SO_3^- \quad \text{(Reaction4)}$$

$$NO_2SO_3^- + H_2O \rightarrow SO_4^{2-} + NO_2^- + 2H^+ \quad \text{(Reaction5)}$$

$$NO_2^- + H^+ \rightarrow HONO_{(g)} \quad \text{(Reaction6)}$$

Here, Reaction 2 is a direct electron transfer from SO_2 hydrate to Cu(II) at aerosol surfaces. Cu(II) with a $3d^9$ outermost electron configuration can delocalize an electron from S(IV), producing SO_3^- radicals and Cu(I) ions[41]. This reaction between S(IV) and Cu(II) is widely applied in water treatment[42,43]. The viability of this reaction has also been confirmed with electron paramagnetic resonance in ref. 35. When this reaction occurs at aerosol surfaces, sulfate formation rate will not be constrained by SO_2

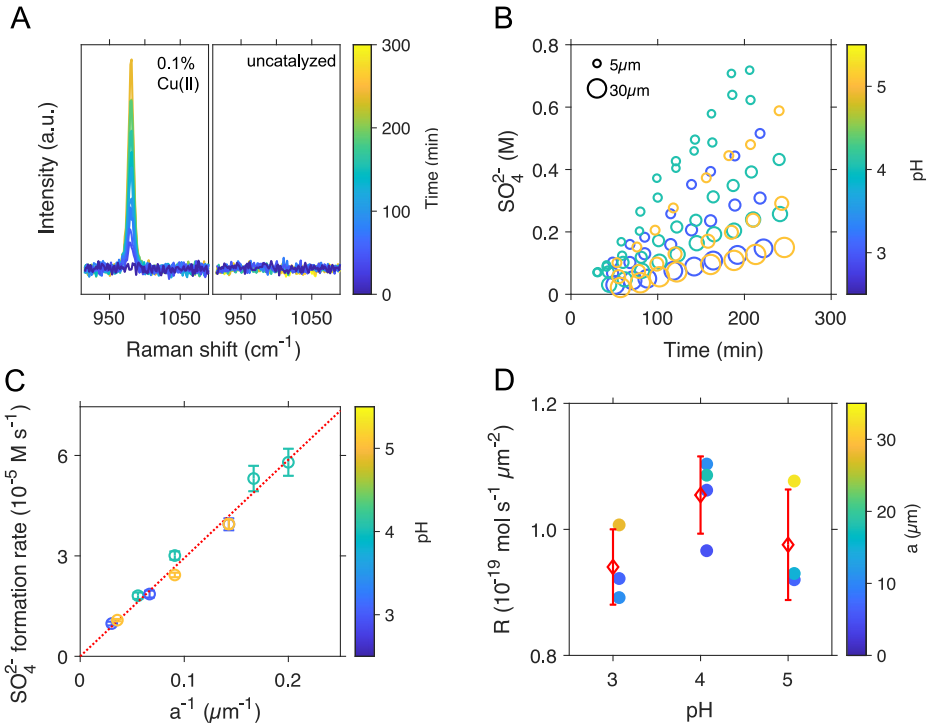

Fig. 1 | Cu-catalyzed oxidation of SO_2 by NO_2 at droplet surface. A In-situ Raman spectra of the microdroplets during the oxidation of SO_2 (500 ppb) by NO_2 (500 ppb). The left panel represents a droplet initially comprising a mixture of $NH_4Cl/HCl/CuCl_2$ (1:0.005:0.001); the reaction was catalyzed by 0.1%Cu-in-solute. The right panel, a droplet initially comprising NH_4Cl/HCl (1:0.005). For both droplets, the pH was buffered at 4 with 400 ppb ambient NH_3. The color indicates reaction time. The peak at 980 cm^{-1} was attributed to SO_4^{2-}. **B–D** Reaction rate determined from Raman microspectrometry (micro-Raman). **B** During reactions, sulfate (SO_4^{2-}) molar concentration increased linearly with time. The size of the circle indicates droplet radius, *a*. The color indicates droplet pH. Conditions were 500 ppb SO_2 and 500 ppb NO_2. Droplets comprised a $NH_4Cl/HCl/CuCl_2$ mixture (1:0.005:0.001) and were buffered at pH approximately 3, 4, or 5 with 40, 400, or 4000 ppb NH_3, respectively. **C** Sulfate formation rate ($d[SO_4^{2-}]/dt$) scales inversely with droplet radius *a* (red dotted line). The color indicates droplet pH. Error bar represents the 95% confident interval values of SO_4^{2-} formation rate, determined by linearly fitting the $[SO_4^{2-}]$ and *t* data. **D** Filled circles represent normalized reaction rate, $R = Vd[SO_4^{2-}]/(Adt)$ (mol sulfate per unit time per unit surface area), which is independent of droplet pH between approximately 3 and 5. The color indicates the droplet radius. Open diamonds and error bars represent the mean and standard deviation values, respectively, of the repeated measurements at each pH condition.

solubility in the bulk aqueous phase. Reaction 3 is an electron transfer from Cu(I) to NO_2, producing NO_2^- and Cu(II), and thus closing the redox cycle. This reaction is thermodynamically viable per the standard potential of the half-reaction (Table S1)[44]. This reaction has also been reported in refs. 35,45 on copper corrosion. Reactions 4 and 5 are radical reactions, in which SO_3^- and NO_2 form $NO_2SO_3^-$ – an intermediate then dissociating into SO_4^{2-} and NO_2^-[14,46]. Reaction 6 is HONO degassing. The overall reaction is illustrated in Fig. 2A.

Considering the short lifetime of the radicals in Reactions 4 and 5, we assumed that Reactions 2 and 3 are rate-limiting steps. Thus, the apparent reaction rate is the rate at which Reaction 2 produces SO_3^-, which scales with the mixing ratio of SO_2, P_{SO_2}, and the aqueous concentration of Cu(II), [Cu(II)]:

$$R = k_2 P_{SO_2}[\mathrm{Cu(II)}] \tag{2}$$

Next, we assumed a steady state for [Cu(II)] and [Cu(I)] ions, such as:

$$k_2 P_{SO_2}[\mathrm{Cu(II)}] = k_3 P_{NO_2}[\mathrm{Cu(I)}] \tag{3}$$

The Eq. 3, when combined with a Cu mass conservation, yields:

$$[\mathrm{Cu(II)}] = [\mathrm{Cu}]\left(1 + \frac{k_2 P_{SO_2}}{k_3 P_{NO_2}}\right)^{-1} \tag{4}$$

Here, $[Cu] = [Cu(I)] + [Cu(II)]$, which is also the initial $[Cu(II)]_{t=0}$ in our experiments. Combining Eqs. 2 and 4, we get the expression of the apparent reaction rate:

$$R = k_2 P_{SO_2}\left(1 + \frac{k_2 P_{SO_2}}{k_3 P_{NO_2}}\right)^{-1}[\mathrm{Cu}] \tag{5}$$

Equation 5 indicates a piecewise trend in the reaction kinetics. Specifically, reaction rate *R* is determined by $k_2 P_{SO_2}[Cu]$, when NO_2 is excessive (i.e., $k_3 P_{NO_2} \gg k_2 P_{SO_2}$); meanwhile, *R* is determined by $k_3 P_{NO_2}[Cu]$, when SO_2 is excessive (i.e., $k_2 P_{SO_2} \gg k_3 P_{NO_2}$). In other words, the apparent kinetics is first-order in either SO_2 or NO_2, depending on which of the gases is excessive. This piece-wise kinetics differs from the second-order kinetics, $R \propto P_{SO_2} P_{NO_2}$, which has been widely used in air-quality models for oxidation of S(IV) by NO_2[8,14,22,23]. The takeaway is that, when the reaction is catalyzed, the redox cycle is bridged by the Cu(I)/Cu(II) ions; the reaction does not occur through a direct interaction between SO_2 and NO_2. As Spindler et al. highlighted in ref. 28, a single-step reaction through a direct S(IV) and NO_2 interaction is thermodynamically unfavorable.

Reaction kinetics

To verify the proposed mechanism, we next measure the rate of $Cu/SO_2/NO_2$ reaction in single droplets levitated by an AOT. Leveraging the cavity-enhanced Raman spectroscopy and the accurate droplet size information obtained from the whispering gallery modes[47], one can measure the sulfate formation by a 10^{-14} mol precision[48,49] in single droplets suspending in the air. These unique advantages allowed us to conduct kinetic experiments at conditions close to the real-world atmosphere, such as a ppb level of reactant

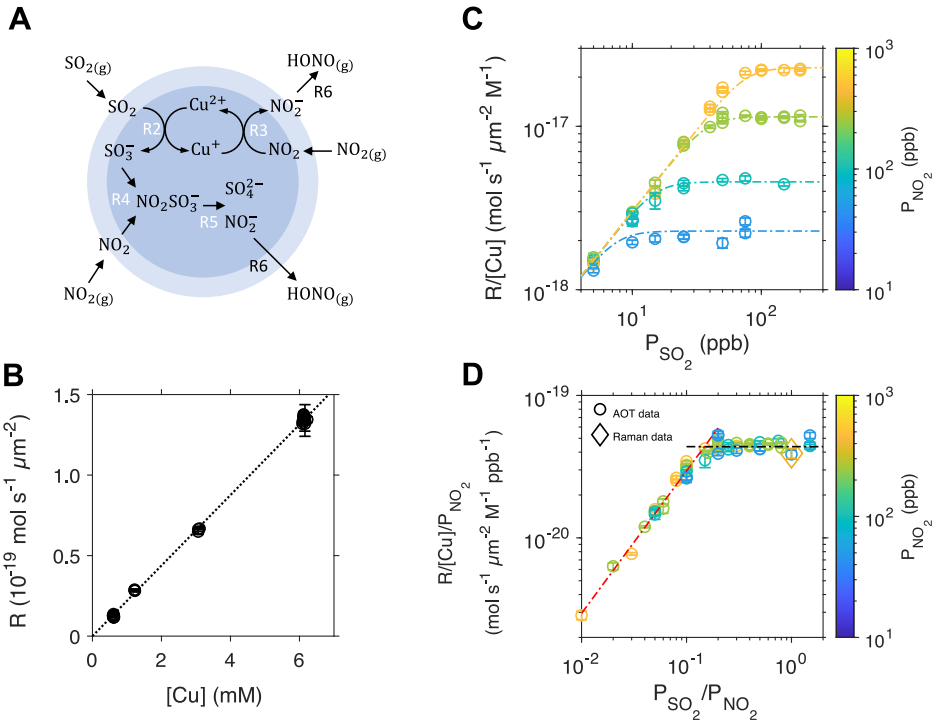

Fig. 2 | Reaction mechanism and kinetics. A A schematic diagram for the reaction mechanism of Cu-catalyzed SO_2 oxidation by NO_2. Reactions 2 and 3 are the rate-limiting steps. R2 stands for Reaction 2 and so forth. **B**–**D** Reaction rate measured with an aerosol optical tweezer (AOT). **B** Normalized reaction rate R increases linearly with the total Cu ions molarity ([Cu], which is also the initial Cu(II) ions molarity). Reaction conditions were 500 ppb SO_2 and 500 ppb NO_2. Droplets initially comprised $(NH_4)_2SO_4/NH_4HSO_4/CuSO_4$ at mixing molar ratio of 1:1:0.0002, 1:1:0.0004, 1:1:0.001, and 1:1:0.002. The droplet was buffered at approximately pH 4 with 800 ppb NH_3. The dotted line represents a linear fit. During reactions, sulfate (SO_4^{2-}) molar concentration increased linearly with time. The size of the circle indicates droplet radius, a. The color indicates droplet pH. Conditions were 500 ppb SO_2 and 500 ppb NO_2. Droplets comprised a $NH_4Cl/HCl/CuCl_2$ mixture (1:0.005:0.001) and were buffered at pH approximately 3, 4, or 5 with 40, 400, or 4000 ppb NH_3, respectively. **C** Normalized reaction rate $R/[Cu]$ is plotted as a function of SO_2 mixing ratio, P_{SO_2} (5–200 ppb). Data are colored per NO_2 mixing ratio, P_{NO_2} (50–500 ppb). Droplets initially comprised a mixture of $(NH_4)_2SO_4/NH_4HSO_4/CuSO_4$ at a mixing molar ratio of 1:1:0.002. The droplet was buffered at approximately pH 4 with 800 ppb NH_3. **D** The same data in **C** is further normalized as $R/([Cu]P_{NO_2})$ versus P_{SO_2}/P_{NO_2}. Also overlaid is the kinetic data determined from the Raman microspectrometry (micro-Raman). The dashed-dotted line illustrates the piecewise trends of the dataset. In **B**–**D**, errors in AOT data arise from the 95% confidence interval values of droplet growth rate determined by analyzing the stimulated Raman spectra (see Methods for details). In **D**, the error in micro-Raman data represents the one standard deviation value of R amongst the 10 measurements shown in Fig.1.

gases and humidity conditions below the deliquescent point of ammonium sulfate.

Figure 2B shows that the reaction rate is first-order in Cu concentration, [Cu], agreeing with our proposed mechanism. Cu(II) will not precipitate in water unless its concentration reaches 220 M at pH 3 or 22 mM at pH 5[34]; these precipitation concentrations are much greater than the actual Cu(II) concentrations in our experiment. Hereafter, we will normalize the reaction rate per $R/[Cu]$. Figure 2C plots $R/[Cu]$ as a function of gases mixing ratio, P_{SO_2} and P_{NO_2}. Specifically, at a fixed P_{NO_2}, there exists a tipping point SO_2 mixing ratio, $P^*_{SO_2}$. When $P_{SO_2} < P^*_{SO_2}$, the reaction rate is linearly proportional to P_{SO_2} but independent of P_{NO_2}; when $P_{SO_2} > P^*_{SO_2}$, the reaction rate is linearly proportional to P_{NO_2} but independent of P_{SO_2}. In other words, the kinetics is piecewise; it is first-order in either SO_2 or NO_2, depending on which of the gases is excessive. The tipping point $P^*_{SO_2}$ is also linearly proportional to P_{NO_2}. Next, we normalize the data and plot in Fig. 2D the relationship between $R/([Cu]P_{NO_2})$ and P_{SO_2}/P_{NO_2}. A universal trend emerges. Such a trend consists of a linearly increasing part, described with $R/[Cu] = k_2 P_{SO_2}$ (red line), and a constant part, described with $R/([Cu]P_{NO_2}) = k_3$ (black line). Extrapolating these trend lines to $P_{SO_2}/P_{NO_2} = 1$ reveals the values of k_2 and k_3. The intersect of these lines reveals the tipping point, $P^*_{SO_2} = (k_3/k_2)P_{NO_2}$. Thus, we write:

$$R = k_2 P_{SO_2}[Cu], \quad \left(P_{SO_2} < \frac{k_3}{k_2} P_{NO_2}\right), \tag{6}$$

$$R = k_3 P_{NO_2}[Cu], \quad \left(P_{SO_2} > \frac{k_3}{k_2} P_{NO_2}\right). \tag{7}$$

where $k_2 = 2.95^{+0.14}_{-0.07} \times 10^{-19}$ and $k_3 = 4.57^{+0.11}_{-0.21} \times 10^{-20}$; both coefficients have a unit of $mol_{S(VI)}\ M_{Cu}^{-1}\ ppb^{-1}\ s^{-1}\ \mu m^{-2}$. Note that k_2 is approximately one order of magnitude greater than k_3. As a result, the tipping point $P^*_{SO_2}$ is about one-tenth of the P_{NO_2} (Fig. 2D). That is, the SO_2 is excessive in this reaction when its concentration is greater than approximately one-tenth of the NO_2 concentration.

Excessive SO_2 in air pollution

In China's urban air pollution, SO_2 and NO_2 concentrations are on the same order of magnitude level. During the severe Beijing haze in January 2013, the average SO_2 and NO_2 mixing ratios were 40 and 66 ppb, respectively[8]. Despite the substantial decrease in SO_2 emission over the past decade, its level is still greater than one-tenth of NO_2 in recent pollution events (Figure S5). Therefore, when sulfate is produced through the Cu-catalyzed reaction pathway, SO_2 remains to be excessive. In other words, the sulfate formation rate would depend on NO_2 concentration, rather than on SO_2 concentration. It may explain why, in field studies[25–27,50], sulfate concentrations were observed to weakly correlate with SO_2 concentration (Fig. 3A), but strongly correlate with NO_2 concentration (Fig. 3B).

When SO_2 is excessive, reducing its concentration *alone* would not be effective in sulfate abatement. For example, China launched in 2013 its Air

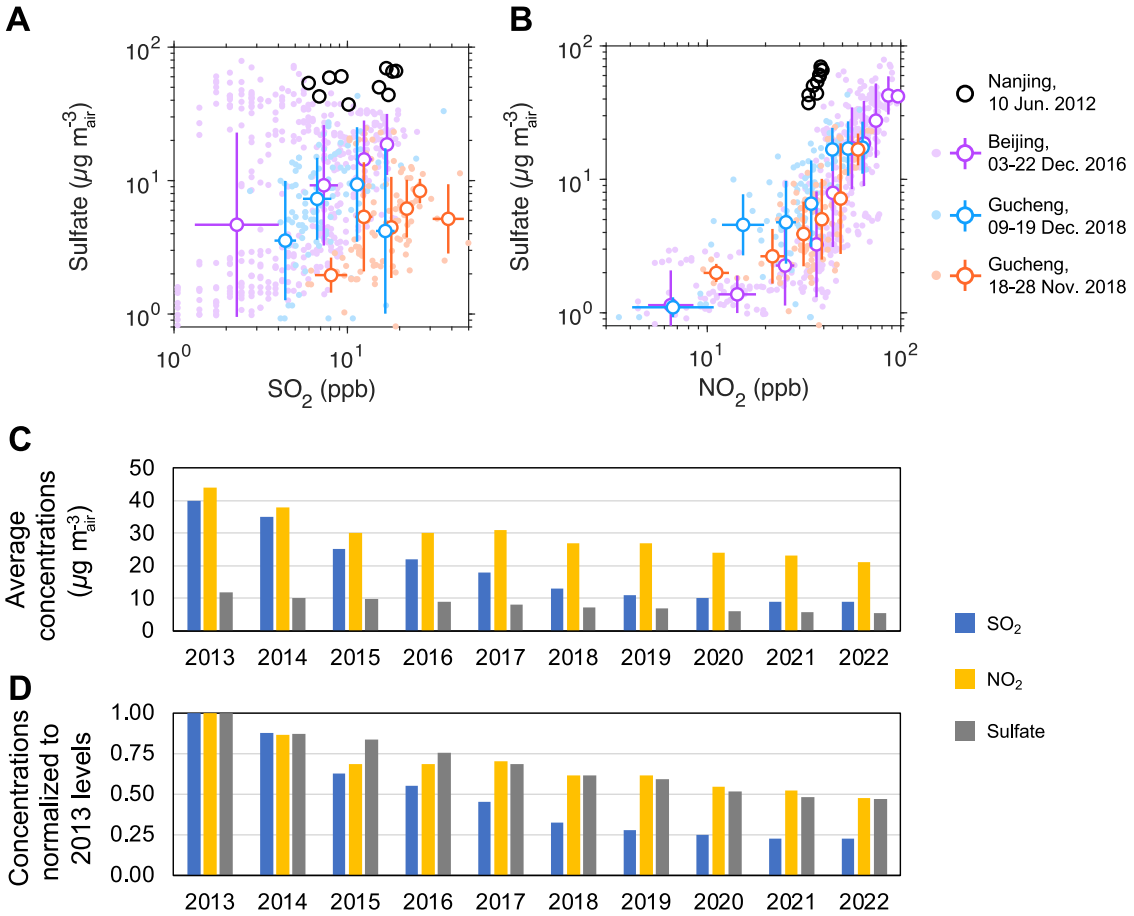

Fig. 3 | Sulfate concentration correlates with NO_2 rather than SO_2. **A**, **B** Sulfate $PM_{2.5}$ concentration as a function of SO_2 and NO_2 mixing ratios, respectively, as reported in past field campaigns conducted in Nanjing[26], Beijing[25], and Hebei at the Gucheng site[50]. Dots represent the data taken from the literature[25,26,50]. Circles with error bars represent the geometric mean and one standard deviation for the data inside each bin (data were binned per the gas mixing ratio, with a 10ppb increment). **C** National annual average concentrations of SO_2 (blue), NO_2 (yellow), and sulfate $PM_{2.5}$ (gray) from 2013 to 2022. The SO_2 and NO_2 concentration data were acquired from the annual *Report on the State of the Ecology and Environment in China*[53] published by the Ministry of Ecology and Environment of the People's Republic of China. The sulfate $PM_{2.5}$ concentration data were acquired from the *Tracking Air Pollution in China* database[54,84] maintained by a team at Tsinghua University. **D** The concentration data in **C** are normalized to their respective values in 2013.

Pollution Prevention and Control Action Plan (hereafter, Action Plan 2013)[51,52], implementing stringent industrial emission standards. As a result, the national annual SO_2 concentration in the ensuing decade has decreased by 77% (Fig. 3C, D)[53]. This substantial decrease in SO_2 emission, however, has *not* led to a proportional decrease in sulfate concentration. Instead, the moderate decrease in sulfate (about 50%) closely matches that in NO_2 (Fig. 3D)[53,54]. This observation again indicates that SO_2 may not be the limiting factor in sulfate formation during urban haze. In other words, sulfate can be produced rapidly at a very low SO_2 concentration, as long as the NO_2 concentration is high. Further abatement faces a greater challenge of reducing NO_2 concentration because NO_2 originates from both industry and traffic emissions, with the latter being a mobile and decentralized source[52].

Copper in polluted air

Traffic is the primary anthropogenic source of Cu in urban areas, such as Beijing[39,55]. Since Cu is an effective heat conductor, it is commonly used as a friction agent in automobile brake pads[56]. A higher Cu concentration was observed in the road dust collected from urban areas with denser traffic[57]. A Beijing campaign[58] showed that the concentration of Cu in the $PM_{2.5}$ sampled at the 4th Ring Road – a major traffic artery in the city – was consistently higher than those sampled at the Tsinghua University campus. A source apportion study[39] reported that brake-and-tire wear contributed 69% of Cu in the $PM_{2.5}$ during the air pollution in Beijing (See Fig. 4A and Table S2).

Yet traffic is not the only source of Cu and NOx in China's air pollution. Industrial processes also contribute significantly to their co-emissions, especially in the broader NCP region[39], i.e., in cities such as Tianjin and those located in the Hebei province (See Fig. 4A and Table S2). In these areas, a significant portion of Cu emissions (36–60%) originates from coal combustions, including power plants and industry boilers[39]. Additionally, in cities such as Tangshan and Handan, a considerable share of Cu (~29%) comes from ferrous metal smelting. Since these industrial processes also emit NOx, it is reasonable to consider Cu and NO_2 as companion emitters across the NCP region. This pairing of the oxidant, NO_2, and the catalyst, Cu, may contribute to the rapid SO_2 conversion observed during haze events (See Fig. 4B)

The Cu concentration in urban air pollution[38,59,60] is considerably higher than that in clean conditions[37] or ambient conditions[61]. During severe haze events in 2014[38], the Cu concentrations in Beijing, Tianjin, and Baoding reached 200, 110, and 190 ng m^{-3}_{air}, respectively (see Fig. 4A and Table S3). The average Cu concentration among the six NCP locations was approximately 119 ± 66 ng m^{-3}_{air} (uncertainty refers to one standard deviation; see Table S3). Next, we assumed an approximately 35% solubility[55] of Cu in aerosol water and a 300 μg m^{-3}_{air} liquid aerosol water content (AWC)[8] in the urban haze. Under these conditions, the concentration of dissolved Cu in

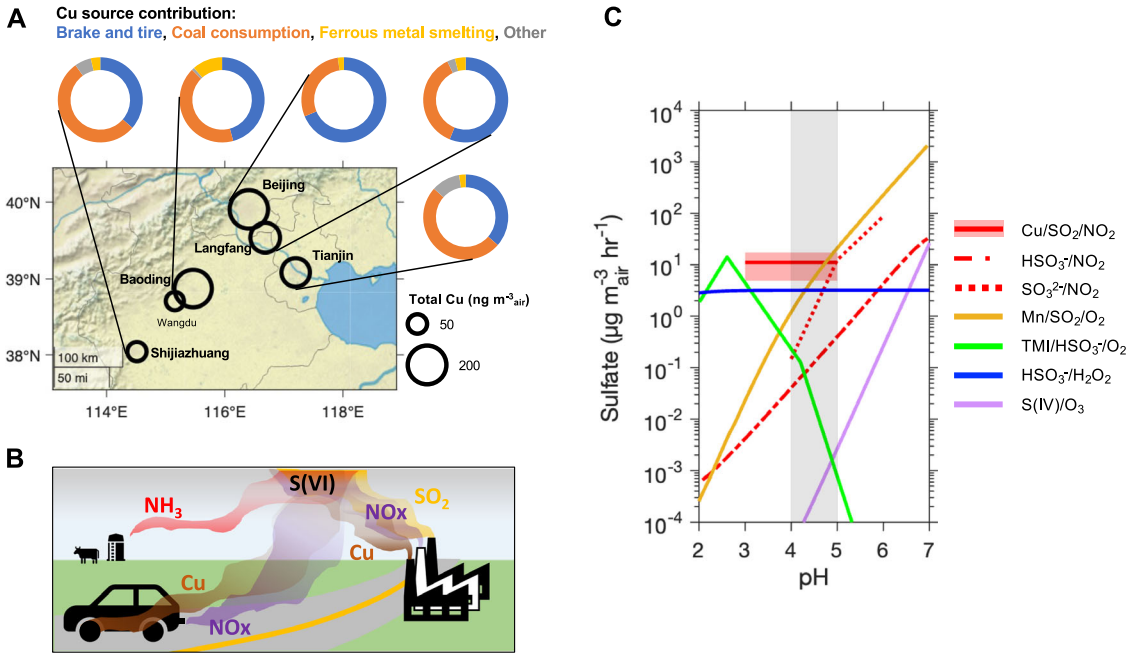

Fig. 4 | Cu-catalyzed SO_2 oxidation by NO_2 as a sulfate source in urban air pollution. **A** The availability of Cu in $PM_{2.5}$ in North China Plain haze events. On the map, circles (size) represent the concentration of total Cu elements in $PM_{2.5}$ during the 2014 haze in Beijing, Tianjin, Langfang, Baoding, and Wangdu, as well as the 2016 haze in Shijiazhuang (See Table S2 for details). Data were acquired from refs. 38,59,60. Surrounding the map are the pie charts for the major Cu sources. Data were acquired from ref. 39. **B** Illustration for the Cu-catalyzed SO_2 oxidation by NO_2 in urban air pollution. **C** Sulfate $PM_{2.5}$ formation rate through various heterogeneous SO_2 oxidation pathways under urban haze conditions. The red solid line represents sulfate formation via the Cu-catalyzed oxidation of SO_2 by NO_2. The rate was estimated by using the kinetics expression in Equation 7. The red-shaded area represents the uncertainty arising from the one standard deviation of Cu concentration in urban air pollution (see Table S3). Also compared here are sulfate formation rates through other reaction pathways reported in literature, including the O_3 pathway (purple curve)[8], H_2O_2 pathway (blue curve)[15], aqueous TMI-catalyzed oxidation (green curve)[15], Mn-catalyzed oxidation on aerosol surface (yellow curve)[13,32], and the uncatalyzed NO_2 pathways (HSO_3^-/NO_2 reaction[8], red dashed-dotted curve; SO_3^{2-}/NO_2 reaction[14], red dotted curve). The conditions for urban haze follow that reported in ref. 8, which include 40 ppb SO_2, 66 ppb NO_2, 0.01 ppb H_2O_2, 1ppb O_3, mean aerosol radius 0.15 μm, and aerosol water content (AWC) 300 μg m^{-3}_{air}. The water-soluble Fe and Mn were 18 and 45 ng m^{-3}_{air}, respectively[32]. The water-soluble and reactive Cu was 34 ± 19 ng m^{-3}_{air}. The gray shaded area represents the pH 4-to-5 range typical to China's urban haze[85,86].

aerosol water is about 2.19 ± 1.22 mM. Details of the calculation can be found in Methods section Supplementary Table S3.

Not all the dissolved Cu species are reactive. Some Cu(II) ions may form complexes with dicarboxylic acids and lose their redox reactivity[62–65]. Following refs. 63,64, we examined the speciation of aqueous Cu(II) in Beijing $PM_{2.5}$ by using the Visual MINTEQ model. The model input included the $PM_{2.5}$ composition data acquired from Beijing campaigns[38,66,67] (See Methods and Supplementary Table S4 and for details). The results show that metal-organic complexes constituted approximately 19% of dissolved Cu(II) in Beijing $PM_{2.5}$. This percentage of metal-organic complexes is slightly lower than those reported from field campaigns at other locations worldwide (Table S5)[62–65]. This is because organic matter constituted a lower mass fraction of $PM_{2.5}$ in NCP haze events, during which the secondary inorganic component and aerosol water content increased substantially[67].

After excluding the metal-organic complexes (19%), we estimated the aqueous concentration of reactive Cu as 1.77 ± 0.99 mM (airborne equivalent concentration, 33.74 ± 18.82 ng m^{-3}_{air}, at AWC of 300 μg m^{-3}_{air}). We also assumed the SO_2 and NO_2 mixing ratios to be 40 and 66 ppb, respectively, per ref. 8. Using these parameters and our kinetic expression in Equation 7, we estimated that the sulfate formation rate via Cu-catalyzed oxidation of SO_2 by NO_2 can reach 11 ± 6 μg m^{-3}_{air} hr^{-1} (Red solid line and shaded area, Fig. 4C). The uncertainty was propagated from the one standard deviation of Cu concentrations reported in NCP field campaigns[38,59,60]. Also overlaid in Fig. 4C are the sulfate production rate via other heterogeneous reaction pathways reported in refs. 8,13–15,32. We highlight the comparison among the NO_2 reaction pathways (Red curves), At acidic conditions, i.e., pH 4, the Cu-catalyzed reaction is faster than the uncatalyzed reactions[8,14] by two to three orders of magnitude. Therefore, the reaction between SO_2 and NO_2 in the urban environment may occur predominately through the Cu-catalyzed route.

Discussion

In the present work, we studied an atmospherically relevant reaction with laboratory experiments. A major limitation of laboratory experiments is that the aerosol reactors cannot fully replicate the atmospheric conditions[68,69], such as the complex aerosol composition in the real world. One potentially important aerosol constituent we did not consider is humic-like substances (HULIS). Under weakly acidic conditions, HULIS—both in protonated and deprotonated forms – can complex with Cu^{2+} ions[70], thereby inhibiting their catalytic activity. Such a kinetic influence of HULIS may also exhibit seasonal variations, since the oxidation state of HULIS determines the distribution of organic functional groups, which in turn affects their complexation tendencies[70]. Without considering the influence of HULIS, our analysis of the sulfate formation rate is prone to overestimation. Additionally, the droplet size in our experiments is slightly larger than $PM_{2.5}$. To account for this mismatch, we normalized reaction rates per the surface area of droplets. This normalized kinetics were then rescaled using the surface area concentration of urban aerosols. This extrapolation remains valid as long as the surface reaction rate is proportional to the area of the air-water interface where the reaction occurs. This extrapolation, however, may not be valid for droplets smaller than 100 nm, as the Kelvin effect becomes significant at that scale. The original data—without normalization and rescaling—may be applicable for polluted fog droplets[19,25] within a similar size range.

Future studies may incorporate the Cu-catalyzed SO_2 oxidation by NO_2 in the atmospheric chemical transport models, so as to better constrain

atmospheric reactions in general. For example, future studies may investigate the synergistic effects of the atmospheric reactions that involve Cu. For example, atmospheric hydroperoxyl (HO_2) radicals can be converted into H_2O_2 through a Cu-catalytic cycle[61,71–73]. This reaction produces H_2O_2 that can in turn oxidize SO_2[15]. HO_2 may also directly participate in the Cu cycle that converts SO_2. Since HO_2 radicals are much more reactive with Cu(I) than with Cu(II)[61], they tend to keep the metal ions at a higher oxidation state, which favors the conversion of SO_2. Another potential oxidant is Fe(III) ions, which can also convert Cu(I) to Cu(II)[61], and such a metal ions synergism may further promote SO_2 conversion. Additionally, for the uncatalyzed reaction between S(IV) and NO_2, we suggest caution on using the second order kinetics, such as $R \propto \left[HSO_3^-\right]\left[NO_2\right]$[22,23], – a formulation widely adopted in the past. This second-order kinetics[22,23] implies a single-step reaction through a direct interaction between HSO_3^- and NO_2, which is unlikely because the redox potentials between these reactants are close[28,29]. Furthermore, the uncatalyzed reaction is unlikely the case because metal ions always exist in urban aerosols, particularly at polluted conditions[34]. And when the redox cycle is bridged by Cu(I)/Cu(II), the reaction kinetics scale with either SO_2 or NO_2, but not with their product.

Electron transfer at the air-water interface is an important mechanism in atmospheric chemistry. Besides sulfate, this mechanism also contributes to the formation of secondary organic aerosols (SOAs). For example, studies by Guzman and coworkers[74–78] have advanced our understanding of the oxidation of phenolic compounds, such as catechol and phenolic aldehydes, by NO_3[75] and OH[74,77] radicals as well as O_3[74,78] at the air-water interface, leading to SOAs. These reactions can also be affected by the presence of TMIs[79]. Understanding these interfacial processes is crucial for evaluating the environmental impacts of biomass burning emissions[76].

We conclude by reiterating the major findings of the present study. First, Cu can catalyze the multiphase SO_2 oxidation by NO_2, accelerating the reaction by up to two orders of magnitude at urban haze conditions. This reaction can be an important but hitherto unknown source of sulfate $PM_{2.5}$ in China haze. This is because, not only is Cu concentration high during urban haze[38], but it is also co-emitted with NO_2 from anthropogenic sources —both industry and traffic[39]. Second, the Cu catalysts also alter the reaction order: When the reaction is Cu-catalyzed, SO_2 tends to be excessive, and the sulfate formation rates scale instead with NO_2 concentration. This observation challenges the widely perceived view that SO_2 is always involved in the rate-limiting step of sulfate $PM_{2.5}$ formation. From a policy perspective, further reducing SO_2 emissions is difficult and may not be effective in sulfate abatement. Instead, cutting off NO_2 emissions from industry and traffic may help further bring down sulfate $PM_{2.5}$ levels. Another practice worth considering is reducing the amount of Cu in automobile brake pads[56], thereby cutting down a catalyst for sulfate formation in the urban atmosphere, such as in Beijing, where traffic contributes to a larger share of both Cu and NOx.

Methods

Micro-Raman experiments

Spectrometer. The measurement was performed with a Renishaw inVia Raman micro-spectrometer. The spectrometer was equipped with a 514.5 nm laser, a Leica DMLM microscope, and an 1800 grooves/mm grating.

Droplets. Droplets were prepared by dispensing solutions onto polytetrafluoroethylene (PTFE) substrates. A medical syringe was used in the dispensing process. When investigating the Cu-catalyzed SO_2 oxidation by NO_2, we prepared the droplets per the following recipes: for the reactions occurring at pH between 3 and 5, the droplets initially comprised a mixture of NH_4Cl/HCl/$CuCl_2$, and these droplets were buffered with NH_3 gas. The molar ratio of NH_4Cl/HCl/$CuCl_2$ was fixed at 1:0.005:0.001. With this recipe, the Cu(II) constituted approximately 0.1% of the solute. In this article, we occasionally denote this mixing arrangement as 0.1%Cu-in-solute. Not to confuse with the weight percent of Cu in aerosols. When investigating the uncatalyzed SO_2 oxidation by NO_2, we prepared the droplets per the following recipe: for the reaction occurring at pH 4, the droplets initially comprised a mixture of NH_4Cl/HCl (1:0.005) and buffered with NH_3. The chemicals, NH_4Cl (purity 99.0%, Beijing Chemical Reagent Factory), $CuCl_2$ (purity 99.99%, Sigma-Aldrich), and HCl (36-38% solution, Beijing Chemical Reagent Factory), were used without further purification.

Droplet ambient conditions. After the droplets were dispensed onto the PTFE substrate, the substrate was loaded into a sample cell. The relative humidity (RH, 77–80%) in the cell was controlled by mixing dry and humidified N_2 gases. The RH was monitored with a hygrometer (CENTER-313, Qunte Technology Co., LTD). The temperature of the sample cell was maintained at room temperature (298 K). Reactants flowed through the sample cell with a prescribed mixing ratio. Specifically, both SO_2 and NO_2 were at 500 ppb. NH_3 was at 40, 400, or 4000 ppb to buffer the NH_4Cl/HCl droplets at pH 3, 4, or 5, respectively. We also conducted parallel experiments in the microdroplets that were unbuffered. In these unbuffered droplets, the formation of sulfurous acids can decrease the droplet pH to a range between ~0 and 1. The detailed experimental conditions for the micro-Raman study can be found in Table S6. Droplet pH was calculated with the extended aerosol inorganic model (E-AIM)[40]. Past studies[80–83] have shown that E-AIM model predicted aerosol pH accurately as long as the compositions of the gas and aqueous phases of aerosols are well characterized. The model does not account for minor species, such as $SO_{2(aq)}$, $SO_2{\cdot}H_2O$, HSO_3^-, and SO_3^{2-}, because S(IV) contribute to pH negligibly compared to SO_4^{2-}.

Raman spectral data collection and analyzes. It took about 20 min before the RH inside the sample cell became stable. After that, we started to collect the Raman spectra of droplet samples. For each droplet sample, the measurement lasted approximately 240 min. The Raman spectra were collected at intervals of about 20 to 30 min. The Raman mode at 980 cm^{-1}, which corresponds to the O-S stretching vibration, was designated to SO_4^{2-}. The Raman mode at 1650 cm^{-1}, which corresponds to the H-O-H bending vibration, was designated to H_2O molecules. We divided the intensity of SO_4^{2-} peak at 980 cm^{-1} with that of H_2O peak at 1650 cm^{-1}, giving a ratio $A_{SO_4^{2-}}/A_{H_2O}$. Such a ratio is linearly proportional to the molar concentration of sulfate ions $[SO_4^{2-}]$. Next, we retrieve the $[SO_4^{2-}]$ by inverting the $A_{SO_4^{2-}}/A_{H_2O}$ with a calibration curve: $A_{SO_4^{2-}}/A_{H_2O} = 0.95 * [SO_4^{2-}]$. We constructed this calibration curve by using the same spectrometer to measure the $A_{SO_4^{2-}}/A_{H_2O}$ of bulk solutions comprising Na_2SO_4 solute with a molar concentration of 0.2, 0.4, 0.6, 0.8, and 1.0 M. In other words, the calibration curve can be used to invert $[SO_4^{2-}]$ below 1.0 M. See Fig. S6 for details of the calibration curve. See Fig.S7 for the Raman spectra of microdroplets during sulfate formation.

Determining reaction kinetics. we performed a linear least-square fitting on the dataset between $[SO_4^{2-}]$ and time, t. The slope was reaction rate, $d[SO_4^{2-}]/t$, on the basis of sulfate molar concentration. Next, the reaction rate R (unit mol s^{-1} μm^{-2}) was calculated by dividing $d[SO_4^{2-}]/t$ with droplet surface area-to-volume ratio, A/V. For each experiment, the values of R, the uncertainties (95% confidence interval values of the linear fitting), and the number of data points used in the fitting can be found in Table S6.

Measuring droplet size. The droplet radius a was measured with the optical microscope equipped with the Raman spectrometer. We assumed droplets to be spheres, with volume $V = \frac{4}{3}\pi a^3$ and surface area $A = 4\pi a^2$. See Fig. S8 for the optical microscope images of the droplets at the extreme size conditions.

AOT experiments

Aerosol optical tweezer. The reaction kinetics were measured in levitated microdroplets with a gradient-force, single-beam AOT. The optical trap was constructed with a 532 nm Gaussian beam, tightly focused with a

100x oil immersion objective scope (Olympus UIS2 PlanCN, numerical aperture of 1.25) inside a 6 mL sample cell. The 532 nm laser constituting the optical trap also served as the incident light for Raman scattering, and the backscattered Raman scattering signal was captured by using a spectrograph (Zolix Ominc λ-500, 1200 grooves/mm grating) with a temporal resolution of one frame per second.

Droplets. Droplets were prepared by aerosolizing solutions with a medical nebulizer (Yuyue 402AI model). When investigating the Cu-catalyzed reaction, we seeded the droplets with a mixture of $(NH_4)_2SO_4$/NH_4HSO_4/$CuSO_4$ at a molar ratio of 1:1:0.0002, 1:1:0.0004, 1:1:0.001, and 1:1:0.002. With these recipes, the Cu(II) respectively constituted 0.01%, 0.02%, 0.05%, and 0.1% of the solute. Again, we occasionally denote, for example, the mixture of $(NH_4)_2SO_4$/NH_4HSO_4/$CuSO_4$ at 1:1:0.002 as 0.1%Cu-in-solute. Not to confuse with the weight percent of Cu in aerosols. When investigating the uncatalyzed reaction, we seeded the droplets with a $(NH_4)_2SO_4$/NH_4HSO_4 mixture (1:1). Chemicals, $(NH_4)_2SO_4$ (purity 99.99%, Sigma-Aldrich), NH_4HSO_4 (purity 99.99%, Sigma-Aldrich), and $CuSO_4$ (99.95%, Sigma-Aldrich), were used without further purification.

Droplet ambient conditions. The aerosolized droplets, led by an N_2 flow, were then delivered to the optical trap inside the sample cell of the AOT system. This sampling process was considered successful when one of the droplets was captured by the optical trap. At this stage, the composition of the droplet is highly sensitive to the ambient gas phase, which should be maintained at stable conditions throughout the measurement. Specifically, the relative humidity (RH, 60 ± 1%) in the cell was controlled by mixing dry and humidified N_2 gases. The RH was monitored with a hygrometer (CENTER-313, Qunte Technology Co., LTD). The temperature was maintained at room temperature (298 K) Reactant gases flowed through the sample cell with a prescribed mixing ratio. When investigating the Cu-catalyzed reaction, we applied the reaction gases per the following arrangements: SO_2 was at 5, 10, 15, 25, 40, 50, 75, 100, 150, or 200 ppb; NO_2 was at 50, 100, 250, or 500 ppb; NH_3 was at 50, 100, 200, 400, or 800 ppb to buffer the $(NH_4)_2SO_4$/NH_4HSO_4 droplets at pH 2.8, 3.1, 3.4, 3.7, or 4.0, respectively. When investigating the uncatalyzed reaction, we applied the gases per the following arrangements: SO_2 was at 0.1, 0.25, 0.5, 0.8, 1.0, 1.5, 2.0, 3.0, 5.0, 7.5, 10.0, or 20.0 ppm; NO_2 was at 10 ppm; NH_3 was at 0.8 or 8.0 ppm to buffer the droplets at pH 4.0 or 5.0 conditions, respectively. The detailed experimental conditions for the AOT study can be found in Table S7. Droplet pH was calculated with E-AIM[40].

Raman spectral data collection and analyzes. The backscattered Raman signal was collected with a time resolution of one second. During the reaction, the SO_2 was continuously converted into SO_4^{2-}, causing a continuous increase in droplet radius, a. Such droplet growth, albeit slight in magnitude, can be precisely determined by observing the redshift of the whispering gallery mode (WGM) in the stimulated Raman spectra. At each time step, t, we inverted the WGM wavelength λ to droplet size a, by using the Mie-scattering calculation algorithm provided in ref. 47. Next, the increase in droplet volume dV, during a time interval dt, can be quantified as:

$$dV = 4\pi a_t^2\left(a_{t+dt} - a_t\right) \quad \text{(EquationS1)}$$

This increase in volume was contributed by the $(NH_4)_2SO_4$ produced by the reaction, and the corresponding increase in the mole of $(NH_4)_2SO_4$ is therefore:

$$dn = \left[(NH_4)_2SO_4\right] * dV \quad \text{(EquationS2)}$$

Here, $\left[(NH_4)_2SO_4\right]$ is the molar concentration at an approximately 60% RH condition, calculated with E-AIM[40]. In summary, the reaction rate can be calculated from droplet growth rate per the following relationships:

$$\frac{dn}{dt}\left(\text{mols}^{-1}\right) = \left[(NH_4)_2SO_4\right] \times \frac{4\pi a_0^2 da}{dt} \times \frac{\text{L}}{10^{15}\mu\text{m}^3} \quad \text{(EquationS3)}$$

and

$$R\left(\text{mols}^{-1}\mu\text{m}^{-1}\right) = \frac{dn}{4\pi a_0^2 * dt} = \left[(NH_4)_2SO_4\right] \times \frac{da}{dt} \times \frac{\text{L}}{10^{15}\mu\text{m}^3} \quad \text{(EquationS4)}$$

Here, a_0 is the initial radius of droplets (unit, μm). The droplet growth rate da/dt (unit, μm s^{-1}) was determined by linearly fitting the $a(t)$ dataset. It is worth noting that Eqs. S1, S3, and S4 hold true only when the value of $a_t - a_0$ is much smaller than a_0 (so that the curvature of the droplet surface can be ignored). In the AOT experiments, the $a_t - a_0$ did not exceed 50 nm, which is approximately 1% of the a_0. For each experiment, the values of da/dt, the uncertainties (95% confidence interval values of the linear fitting), and the number of data points used in the fitting can be found in Table S7. Also, note that the treatment of Eqs. S3 and S4 requires that SO_4^{2-} is the sole product remaining in the condensed phase. Such a condition has been confirmed in our Micro-Raman study (See Fig.S7). We also assumed that the product was always $(NH_4)_2SO_4$ when NH_3 was in the ambient gases.

Aqueous copper speciation model

Visual MINTEQ. Following the method introduced in refs. 63,64, we estimated the chemical speciations of Cu(II) in the aqueous phase of Beijing $PM_{2.5}$ by using Visual MINTEQ model version 3.1. The visual MINTEQ model, which was originally designed for chemical speciation analysis in natural aquatic systems, has also been successfully utilized for estimating metal speciation in aerosol water[63,64]. In other words, this model accounts for metal-organic complex formation and calculates the fraction of metals existing as organic complexes. The model input parameters included the aqueous concentrations of secondary inorganic matters (SO_4^{2-}, NO_3^-, and NH_4^+), dicarboxylic acids (oxalate, malonate, succinate, and glutarate), and metal ions (Na^+, K^+, Mg^{2+}, Ca^{2+}, Al^{3+}, Mn^{2+}, As^{3+}, Cr^{2+}, Cu^{2+}, Ni^{2+}, Pb^{2+}, Sb^{3+}, Se^{4+}, Zn^{2+}, Fe^{2+}, and Fe^{3+}), as well as aqueous pH (fixed at 4) and temperature (fixed at 25 °C). These $PM_{2.5}$ composition data were acquired from field campaigns conducted in Beijing[38,66,67]. Details of the composition data can be found in Table S4. Following that recommended in ref. 64, we adopted the specific interaction theory (SIT) for the ionic strength correction of the stability constants of the metal complexes. SIT correction was preferred because it is more appropriate for the high ionic strength condition (>1 M) of urban aerosols[64].

Sulfate, nitrate, and ammonium. We estimated the aqueous concentrations of inorganic matters with the E-AIM model[40] according to the hygroscopicity of a SO_4^{2-}/NO_3^-/NH_4^+ mixture at a molar ratio of 1:1.5:3.5 and at an ambient RH of 80%. The molar ratio of the mixture was determined according to the mass fractions of SO_4^{2-} (19.2%), NO_3^- (18.5%), and NH_4^+ (12.6%) in Beijing $PM_{2.5}$ at heavily polluted conditions[67].

Dicarboxylic acids. We took the concentration of dicarboxylic acids in Beijing $PM_{2.5}$ from ref. 66 (Winter data, December 2013, Beijing Campaign, See Table S4). Then we calculated the aqueous concentrations (unit: mol kg^{-1}) of the dicarboxylic acids by using their atmospheric concentrations (unit: ng m^{-3}_{air}), molar mass (unit: g mol^{-1}), and atmospheric water contents, AWC, (300 μg m^{-3}_{air})[8].

Metals. We took the atmospheric concentration of metals in Beijing $PM_{2.5}$ from ref. 38 (Winter data, January 2014, Beijing Campaign, See Table S4). Similarly, we calculated the aqueous concentrations (unit: mol kg^{-1}) of the metals by using their atmospheric concentrations

(unit: ng m^{-3}_{air}), molar mass (unit: g mol^{-1}), and atmospheric water contents, AWC, (300 μg m^{-3}_{air})[8]. The oxidation state of metal ions was assigned as follows: Al^{3+}, Mn^{2+}, As^{3+}, Cr^{2+}, Cu^{2+}, Ni^{2+}, Pb^{2+}, Sb^{3+}, Se^{4+}, Zn^{2+}, Fe^{2+}, and Fe^{3+}. The Fe^{2+} and Fe^{3+} were assumed to exist in equal amounts, per ref. 64. During calculation, the species that were predicted to be in an oversaturation state were allowed to precipitate[63,64].

Calculating sulfate formation rates at urban haze conditions

Reactive Cu in aqueous phase. Table S3 provides the total Cu (ng m^{-3}_{air}) in the $PM_{2.5}$ during past NCP haze events[38,59,60]. The total Cu refers to all forms of Cu elements existing in the $PM_{2.5}$ sample, including both the water-soluble and insoluble fractions. The soluble fraction can be calculated by multiplying total Cu with the solubility of Cu (hereafter, f_S). A field campaign in China[55] shows $f_S \approx 35\%$ in acidic aerosol water. Among the soluble Cu, we assume that the fraction forming metal organic complexes ($f_{OM} \approx 19\%$, See Table S5) are non-reactive. That is, the reactive fraction can be calculated by multiplying soluble Cu with $1 - f_{OM}$. To summarize, we write the following equation for reactive Cu concentration in the aqueous phase:

$$[\mathrm{Cu}](\mathrm{mM}) = f_S \times (1 - f_{OM}) \times \frac{\mathrm{Cu}\left(\mathrm{ng\,m_{air}^{-3}}\right)}{M_{w,Cu}\left(\mathrm{g\,mol^{-1}}\right) \times \mathrm{AWC}\left(\mathrm{L\,m_{air}^{-3}}\right)} \times \frac{10^{-9}\mathrm{g}}{\mathrm{ng}} \times \frac{10^{3}\mathrm{mmol}}{\mathrm{mol}} \quad \text{(S5)}$$

$$\mathrm{AWC}\left(\mathrm{L\,m_{air}^{-3}}\right) = \frac{\mathrm{PM}_{2.5}\left(\mu\mathrm{g\,m_{air}^{-3}}\right)}{\rho_{water}\left(\mathrm{kg\,m^{-3}}\right)} \times \frac{10^{-9}\mathrm{kg}}{\mu\mathrm{g}} \times \frac{10^{3}\mathrm{L}}{m^{3}} \quad \text{(S6)}$$

Here, $M_{w,Cu}$ (63.55 g mol^{-1}) is copper molecular weight; The AWC (L m^{-3}_{air}) refers to the volume of aerosol liquid water content per unit volume of air. For simplicity, we calculated the AWC (L m^{-3}_{air}) by dividing the AWC (300 μg m^{-3}_{air}) with water density ρ_{water} (10^3 kg m^{-3}) (See Eq. S6). Refer to Table S5 for the concentrations of soluble and soluble-and-reactive Cu in Beijing $PM_{2.5}$. Note that the aqueous [Cu] is on the order of millimolar level, which is three orders of magnitude lower than the $Cu(OH)_2$ precipitation limit at pH 4 (approximately 2.2 M)[34]. Thus, the aqueous [Cu] concentration in urban aerosols can be regarded as pH-independent.

Extrapolation of reaction kinetics

The urban air pollution conditions follow that reported in ref. 8. Specifically, the average aerosol radius (a) was 0.15 μm, SO_2 mixing ratio P_{SO_2}, 40 ppb; NO_2 mixing ratio P_{NO_2}, 66 ppb; The mass concentration of AWC, 300 μg m^{-3}_{air}. Since SO_2 mixing ratio is much greater than the tipping point mixing ratio, i.e., $P_{SO_2} > (k_2/k_1)P_{NO_2}$, the kinetic formulation in Equation 7 (in main text) was used to calculate sulfate formation rate at urban haze conditions. The reactive [Cu] concentration was calculated with Eq. S5. The resultant reaction rate R (unit: mol s^{-1} μm^{-2}) was then extrapolated to an atmospheric sulfate formation rate (unit, μg m^{-3}_{air} hr^{-1}), with the knowledge of sulfate molecular weight $M_{w,S(VI)}$ (96.06 g mol^{-1}), AWC (300 μg m^{-3}_{air}), average aerosol radius a (0.15 μm), and water density ρ_{water} (10^3 kg m^{-3}), specifically:

$$R\left(\mu\mathrm{g\,m_{air}^{-3}\,hr^{-1}}\right) = R\left(\mathrm{mol\,s^{-1}\,\mu m^{-2}}\right) \times M_{w,S(VI)}\left(\mathrm{g\,mol^{-1}}\right) \times \widetilde{A}\left(\mu\mathrm{m^2\,m_{air}^{-3}}\right) \times \frac{10^{6}\mu\mathrm{g}}{\mathrm{g}} \times \frac{3600\mathrm{s}}{\mathrm{hr}} \quad \text{(S7)}$$

$$\widetilde{A}\left(\mu\mathrm{m^2\,m_{air}^{-3}}\right) = 4\pi a^2\left(\mu\mathrm{m^2}\right) \times \mathrm{AWC}\left(\mu\mathrm{g\,m_{air}^{-3}}\right) \times m^{-1}\left(\mu\mathrm{g^{-1}}\right) \quad \text{(S8)}$$

and

$$m(\mu\mathrm{g}) = \frac{4}{3}\pi a^3\left(\mu\mathrm{m^3}\right) \times \rho_{water}\left(\mathrm{kg\,m^{-3}}\right) \times \left(\frac{10^{-6}\mathrm{m}}{\mu\mathrm{m}}\right)^3 \times \frac{10^{9}\mu\mathrm{g}}{\mathrm{kg}} \quad \text{(S9)}$$

Here, $\widetilde{A}\left(\mu\mathrm{m^2\,m_{air}^{-3}}\right)$ is aerosol surface area per unit air volume; m (μg) is the mass of a single aerosol particle.

Data availability

All the original data generated in this study has been uploaded to Mendeley Data and can be accessed through the link: http://www.doi.org/10.17632/32897xmjkr.1.

Code availability

This work did not generate any original code.

Received: 21 October 2024; Accepted: 2 February 2025;
Published online: 18 February 2025

References

1. Huang, R.-J. et al. High secondary aerosol contribution to particulate pollution during haze events in China. *Nature* **514**, 218–222 (2014).
2. Zhang, R. et al. Formation of urban fine particulate matter. *Chem. Rev.* **115**, 3803–3855 (2015).
3. Guo, S. et al. Elucidating severe urban haze formation in China. *Proc. Natl. Acad. Sci. USA* **111**, 17373–17378 (2014).
4. Murray, C. J. et al. Global burden of 87 risk factors in 204 countries and territories, 1990–2019: A systematic analysis for the Global Burden of Disease Study 2019. *Lancet* **396**, 1223–1249 (2020).
5. Southerland, V. A. et al. Global urban temporal trends in fine particulate matter ($PM_{2.5}$) and attributable health burdens: Estimates from global datasets. *Lancet Planet. Health* **6**, e139–e146 (2022).
6. National Development and Reform Commission, State Council of the People's Republic of China. The 14th Five-Year Plan and Long-Range Objectives through 2035. Chapter 38, Section 1. https://en.ndrc.gov.cn/policies/202303/P020230425398570720357.pdf.
7. Wang, G. et al. Persistent sulfate formation from London Fog to Chinese haze. *Proc. Natl. Acad. Sci. USA* **113**, 13630–13635 (2016).
8. Cheng, Y. et al. Reactive nitrogen chemistry in aerosol water as a source of sulfate during haze events in China. *Sci. Adv.* **2**, e1601530 (2016).
9. Liu, C., Ma, Q., Liu, Y., Ma, J. & He, H. Synergistic reaction between SO_2 and NO_2 on mineral oxides: A potential formation pathway of sulfate aerosol. *Phys. Chem. Chem. Phys.* **14**, 1668–1676 (2012).
10. He, H. *et al*. SO_2 over central China: Measurements, numerical simulations and the tropospheric sulfur budget. *J. Geophys. Res. Atmos*. **117** https://doi.org/10.1029/2011JD016473 (2012)
11. Wang, Y., Zhang, Q., He, K., Zhang, Q. & Chai, L. Sulfate-nitrate-ammonium aerosols over China: Response to 2000–2015 emission changes of sulfur dioxide, nitrogen oxides, and ammonia. *Atmos. Chem. Phys.* **13**, 2635–2652 (2013).
12. Liu, X. et al. Enhanced nitrogen deposition over China. *Nature* **494**, 459–462 (2013).
13. Wang, W. et al. Sulfate formation is dominated by manganese-catalyzed oxidation of SO_2 on aerosol surfaces during haze events. *Nat. Comm.* **12**, 1–10 (2021).
14. Liu, T. & Abbatt, J. P. Oxidation of sulfur dioxide by nitrogen dioxide accelerated at the interface of deliquesced aerosol particles. *Nat. Chem.* **13**, 1173–1177 (2021).
15. Liu, T., Clegg, S. L. & Abbatt, J. P. Fast oxidation of sulfur dioxide by hydrogen peroxide in deliquesced aerosol particles. *Proc. Natl. Acad. Sci. USA* **117**, 1354–1359 (2020).
16. Ruiz-Lopez, M. F., Francisco, J. S., Martins-Costa, M. T. & Anglada, J. M. Molecular reactions at aqueous interfaces. *Nat. Rev. Chem.* **4**, 459–475 (2020).
17. Li, L.-F. et al. Rethinking urban haze formation: atmospheric sulfite conversion rate scales with aerosol surface area, not volume. *One Earth* **7**, 1082–1095 (2024).
18. Angle, K. J., Neal, E. E. & Grassian, V. H. Enhanced rates of transition-metal-ion-catalyzed oxidation of S(IV) in aqueous aerosols: Insights into sulfate aerosol formation in the atmosphere. *Environ. Sci. Technol.* **55**, 10291–10299 (2021).
19. Herrmann, H. Kinetics of aqueous phase reactions relevant for atmospheric chemistry. *Chem. Rev.* **103**, 4691–4716 (2003).

20. Ma, Q. et al. A review on the heterogeneous oxidation of SO_2 on solid atmospheric particles: Implications for sulfate formation in haze chemistry. *Crit. Rev. Environ. Sci. Technol.* **53**, 1888–1911 (2023).
21. Zhang, P. et al. Insight into the mechanism and kinetics of the heterogeneous reaction between SO_2 and NO_2 on diesel black carbon under light irradiation. *Environ. Sci. Technol.* **57**, 17718–17726 (2023).
22. Clifton, C. L., Altstein, N. & Huie, R. E. Rate constant for the reaction of nitrogen dioxide with sulfur(IV) over the pH range 5.3-13. *Environ. Sci. Technol.* **22**, 586–589 (1988).
23. Lee, Y. N. & Schwartz, S. E. in *Precipitation Scavenging, Dry Deposition, and Resuspension* Vol. 1 453-470 (New York: Elsevier, 1983).
24. Littlejohn, D., Wang, Y. & Chang, S. G. Oxidation of aqueous sulfite ion by nitrogen dioxide. *Environ. Sci. Technol.* **27**, 2162–2167 (1993).
25. Wang, J. et al. Fast sulfate formation from oxidation of SO_2 by NO_2 and HONO observed in Beijing haze. *Nat. Comm.* **11**, 1–7 (2020).
26. Xie, Y. et al. Enhanced sulfate formation by nitrogen dioxide: implications from in situ observations at the SORPES station. *J. Geophys. Res. Atmos.* **120**, 12679–12694 (2015).
27. Ding, A. J. et al. Intense atmospheric pollution modifies weather: a case of mixed biomass burning with fossil fuel combustion pollution in eastern China. *Atmos. Chem. Phys.* **13**, 10545–10554 (2013).
28. Spindler, G. et al. Wet annular denuder measurements of nitrous acid: laboratory study of the artefact reaction of NO_2 with S(IV) in aqueous solution and comparison with field measurements. *Atmos. Environ.* **37**, 2643–2662 (2003).
29. Tilgner, A. et al. Acidity and the multiphase chemistry of atmospheric aqueous particles and clouds. *Atmos. Chem. Phys.* **21**, 13483–13536 (2021).
30. Pye, H. O. T. et al. The acidity of atmospheric particles and clouds. *Atmos. Chem. Phys.* **20**, 4809–4888 (2020).
31. Wang, T. et al. Significant formation of sulfate aerosols contributed by the heterogeneous drivers of dust surface. *Atmos. Chem. Phys.* **22**, 13467–13493 (2022).
32. Wang, T. et al. Sulfate formation apportionment during winter haze events in north China. *Environ. Sci. Technol.* **56**, 7771–7778 (2022).
33. Gao, J. et al. Hydrogen peroxide serves as pivotal fountainhead for aerosol aqueous sulfate formation from a global perspective. *Nat. Comm.* **15**, 4625 (2024).
34. Graedel, T. & Weschler, C. Chemistry within aqueous atmospheric aerosols and raindrops. *Rev. Geophys.* **19**, 505–539 (1981).
35. Liu, S., Lian, Z., Zhang, M., Zhang, S. & Zhong, Q. Intensification of NO_2 removal in sulfite solutions with reusable copper chloride: Mechanism and process parameters. *Sep. Purif. Technol.* **308**, 122996 (2023).
36. Xiong, Y. et al. Efficient inhibition of N_2O during NO absorption process using a CuO and $(NH_4)_2SO_3$ mixed solution. *Ind. Eng. Chem. Res.* **57**, 13010–13018 (2018).
37. Cui, Y. et al. Characteristics and sources of hourly trace elements in airborne fine particles in urban Beijing, China. *J. Geophys. Res. Atmos.* **124**, 11595–11613 (2019).
38. Gao, J. et al. Temporal-spatial characteristics and source apportionment of $PM_{2.5}$ as well as its associated chemical species in the Beijing-Tianjin-Hebei region of China. *Environ. Pollut.* **233**, 714–724 (2018).
39. Zhu, C. et al. A high-resolution emission inventory of anthropogenic trace elements in Beijing-Tianjin-Hebei (BTH) region of China. *Atmos. Environ.* **191**, 452–462 (2018).
40. Wexler, A. S. & Clegg, S. L. Atmospheric aerosol models for systems including the ions H^+, NH_4^+, Na^+, SO_4^{2-}, NO_3^-, Cl^-, Br^-, and H_2O. *J. Geophys. Res. Atmos.* **107**, ACH 14-11–ACH 14-14 (2002).
41. Cheng, R. T., Corn, M. & Frohliger, J. O. Contribution to the reaction kinetics of water soluble aerosols and SO_2 in air at ppm concentrations. *Atmos. Environ. (1967)* **5**, 987–1008 (1971).
42. Chen, L. et al. Efficient bacterial inactivation by transition metal catalyzed auto-oxidation of sulfite. *Environ. Sci. Technol.* **51**, 12663–12671 (2017).
43. Wu, S., Shen, L., Lin, Y., Yin, K. & Yang, C. Sulfite-based advanced oxidation and reduction processes for water treatment. *Chem. Eng. J.* **414**, 128872 (2021).
44. Atkins, P., de Paula, J. & Keeler, J. *Atkins' Physical Chemistry*. 11th edn, 880-882 (New York: Oxford University Press, 2014).
45. Persson, D. & Leygraf, C. Vibrational spectroscopy and XPS for atmospheric corrosion studies on copper. *J. Electrochem. Soc.* **137**, 3163–3169 (1990).
46. Yang, J. et al. Unraveling a new chemical mechanism of missing sulfate formation in aerosol haze: gaseous NO_2 with aqueous HSO_3^-/SO_3^{2-}. *J. Am. Chem. Soc.* **141**, 19312–19320 (2019).
47. Preston, T. C. & Reid, J. P. Accurate and efficient determination of the radius, refractive index, and dispersion of weakly absorbing spherical particle using whispering gallery modes. *J. Opt. Soc. Am. B* **30**, 2113–2122 (2013).
48. Cao, X. et al. Directly measuring Fe(III)-catalyzed SO_2 oxidation rate in single optically levitated droplets. *Environ. Sci. Atmos.* **3**, 298–304 (2023).
49. Chen, Z. et al. Rapid sulfate formation via uncatalyzed autoxidation of sulfur dioxide in aerosol microdroplets. *Environ. Sci. Technol.* **56**, 7637–7646 (2022).
50. Li, G. et al. Multiphase chemistry experiment in Fogs and Aerosols in the North China Plain (McFAN): Integrated analysis and intensive winter campaign 2018. *Faraday Discuss.* **226**, 207–222 (2021).
51. State Council of the People's Republic of China, Notice of the general office of the state council on issuing the air pollution prevention and control action plan (in Chinese). http://www.gov.cn/zwgk/2013-09/12/content_2486773.htm.
52. Zhang, Q. et al. Drivers of improved $PM_{2.5}$ air quality in China from 2013 to 2017. *Proc. Natl. Acad. Sci. USA* **116**, 24463–24469 (2019).
53. Ministry of Ecology and Environment of the People's Republic of China. Report on the State of the Ecology and Environment in China. http://english.mee.gov.cn/Resources/Reports/soe/.
54. Tracking Air Pollution in China (TAP) database. http://tapdata.org.cn/?page_id=523&lang=en.
55. Liu, M. et al. High fraction of soluble trace metals in fine particles under heavy haze in central China. *Sci. Total Environ.* **841**, 156771 (2022).
56. Jeong, H., Ryu, J.-S. & Ra, K. Characteristics of potentially toxic elements and multi-isotope signatures (Cu, Zn, Pb) in non-exhaust traffic emission sources. *Environ. Pollut.* **292**, 118339 (2022).
57. Zhao, G. et al. Pollution characteristics, spatial distribution, and source identification of heavy metals in road dust in a central eastern city in China: A comprehensive survey. *Environ. Monit. Assess.* **193**, 1–13 (2021).
58. Duan, J., Tan, J., Wang, S., Hao, J. & Chai, F. Size distributions and sources of elements in particulate matter at curbside, urban and rural sites in Beijing. *J. Environ. Sci.* **24**, 87–94 (2012).
59. Song, H. et al. Influence of aerosol copper on HO_2 uptake: a novel parameterized equation. *Atmos. Chem. Phys.* **20**, 15835–15850 (2020).
60. Chen, F. et al. Chemical characteristics of $PM_{2.5}$ during a 2016 winter haze episode in Shijiazhuang, China. *Aerosol Air Qual. Res.* **17**, 368–380 (2017).
61. Mao, J., Fan, S., Jacob, D. J. & Travis, K. R. Radical loss in the atmosphere from Cu-Fe redox coupling in aerosols. *Atmos. Chem. Phys.* **13**, 509–519 (2013).
62. Li, T. et al. Evolution of trace elements in the planetary boundary layer in southern China: Effects of dust storms and aerosol-cloud interactions. *J. Geophys. Res. Atmos.* **122**, 3492–3506 (2017).
63. Scheinhardt, S., Müller, K., Spindler, G. & Herrmann, H. Complexation of trace metals in size-segregated aerosol particles at nine sites in Germany. *Atmos. Environ.* **74**, 102–109 (2013).
64. Shahpoury, P. et al. Influence of aerosol acidity and organic ligands on transition metal solubility and oxidative potential of fine particulate matter in urban environments. *Sci. Total Environ.* **906**, 167405 (2023).

65. Tapparo, A. et al. Formation of metal-organic ligand complexes affects solubility of metals in airborne particles at an urban site in the Po valley. *Chemosphere* **241**, 125025 (2020).
66. Zhao, W. et al. Molecular distribution and compound-specific stable carbon isotopic composition of dicarboxylic acids, oxocarboxylic acids and α-dicarbonyls in $PM_{2.5}$ from Beijing, China. *Atmos. Chem. Phys.* **18**, 2749–2767 (2018).
67. Zheng, G. J. et al. Exploring the severe winter haze in Beijing: the impact of synoptic weather, regional transport and heterogeneous reactions. *Atmos. Chem. Phys.* **15**, 2969–2983 (2015).
68. Liu, T., Chan, A. W. & Abbatt, J. P. Multiphase oxidation of sulfur dioxide in aerosol particles: Implications for sulfate formation in polluted environments. *Environ. Sci. Technol.* **55**, 4227–4242 (2021).
69. Su, H., Cheng, Y. & Pöschl, U. New multiphase chemical processes influencing atmospheric aerosols, air quality, and climate in the anthropocene. *Acc. Chem. Res.* **53**, 2034–2043 (2020).
70. Qin, J. et al. Measurement report: Effects of transition metal ions on the optical properties of humic-like substances (HULIS) reveal a structural preference – a case study of PM2.5 in Beijing, China. *Atmos. Chem. Phys.* **24**, 7575–7589 (2024).
71. Mozurkewich, M., McMurry, P. H., Gupta, A. & Calvert, J. G. Mass accommodation coefficient for HO_2 radicals on aqueous particles. *J. Geophys. Res. Atmos.* **92**, 4163–4170 (1987).
72. Taketani, F. et al. Measurement of overall uptake coefficients for HO_2 radicals by aerosol particles sampled from ambient air at Mts. Tai and Mang (China). *Atmos. Chem. Phys.* **12**, 11907–11916 (2012).
73. Thornton, J. & Abbatt, J. P. Measurements of HO_2 uptake to aqueous aerosol: Mass accommodation coefficients and net reactive loss. *J. Geophys. Res. Atmos*. **110** (2005).
74. Pillar-Little, E. A., Camm, R. C. & Guzman, M. I. Catechol oxidation by ozone and hydroxyl radicals at the air–water interface. *Environ. Sci. Technol.* **48**, 14352–14360 (2014).
75. Rana, M. S. & Guzman, M. I. Oxidation of catechols at the air–water interface by nitrate radicals. *Environ. Sci. Technol.* **56**, 15437–15448 (2022).
76. Guzman, M. I., Pillar-Little, E. A. & Eugene, A. J. Interfacial oxidative oligomerization of catechol. *ACS Omega* **7**, 36009–36016 (2022).
77. Rana, M. S. & Guzman, M. I. Oxidation of phenolic aldehydes by ozone and hydroxyl radicals at the air–water interface. *J. Phys. Chem. A* **124**, 8822–8833 (2020).
78. Rana, M. S., Bradley, S. T. & Guzman, M. I. Conversion of catechol to 4-nitrocatechol in aqueous Microdroplets Exposed to O_3 and NO_2. *ACS ES&T Air* **1**, 80–91 (2024).
79. Al-Abadleh, H. A. et al. Reactivity of aminophenols in forming nitrogen-containing brown carbon from iron-catalyzed reactions. *Commun. Chem.* **5**, 112 (2022).
80. Boyer, H. C., Gorkowski, K. & Sullivan, R. C. In situ pH measurements of individual levitated microdroplets using aerosol optical tweezers. *Anal. Chem.* **92**, 1089–1096 (2020).
81. Jing, X., Chen, Z., Huang, Q., Liu, P. & Zhang, Y.-H. Spatiotemporally resolved pH measurement in aerosol microdroplets undergoing chloride depletion: An application of in situ Raman microspectrometry. *Anal. Chem.* **94**, 15132–15138 (2022).
82. Li, M. et al. Aerosol pH and ion activities of HSO_4^- and SO_4^{2-} in supersaturated single droplets. *Environ. Sci. Technol.* **56**, 12863–12872 (2022).
83. Li, L.-F., Chen, Z., Liu, P. & Zhang, Y.-H. Direct measurement of pH evolution in aerosol microdroplets undergoing ammonium depletion: A surface-enhanced Raman spectroscopy approach. *Environ. Sci. Technol.* **56**, 6274–6281 (2022).
84. Geng, G. et al. Tracking air pollution in China: Near real-time $PM_{2.5}$ retrievals from multisource data fusion. *Environ. Sci. Technol.* **55**, 12106–12115 (2021).
85. Song, S. et al. Fine-particle pH for Beijing winter haze as inferred from different thermodynamic equilibrium models. *Atmos. Chem. Phys.* **18**, 7423–7438 (2018).
86. Liu, M. et al. Fine particle pH during severe haze episodes in northern China. *Geophys. Res. Lett.* **44**, 5213–5221 (2017).

Acknowledgements

We thank Prof. Hong He, Prof. Qingxin Ma, and Prof. Peng Zhang at Research Center for Eco-Environmental Sciences, Chinese Academy of Sciences, for discussing the haze chemistry in general and the multiphase SO_2 conversion in specific. We thank Prof. Jonathan P. Reid at the University of Bristol for helping us set up the aerosol optical tweezer. We thank Prof. Nan Ma at Jinan University, Prof. Hang Su at Institute of Atmospheric Physics, Chinese Academy of Sciences, and Prof. Yafang Cheng at the Max Planck Institute for Chemistry for granting us access to the dataset of the field campaign at Gucheng, Hebei, China. This research has been supported by the National Natural Science Foundation of China (Nos. 42127806, 22321004, 22376014, and 42205113) and Beijing Institute of Technology Research Fund Program for Young Scholars.

Author contributions

Conceptualization: P.L., Q.H., Y.Z., M.G. Methodology: P.L., Q.H., Z.C., S.P., W.W., Y.Z., M.G. Investigation: Y.L., L.L., X.K., P.L., M.Z., J.Y., Q.H., Z.C., X.Z., X.C., W.W., Y.Z., M.G. Visualization: P.L., Q.H., Y.Z., M.G. Funding acquisition: P.L., Q.H., Y.Z., M.G. Supervision: Y.Z., M.G. Writing (original draft): P.L., Q.H. Writing (review and editing): P.L., Q.H., W.W., Y.Z., M.G.

Competing interests

The authors declare no competing interests.

Additional information

Supplementary information The online version contains supplementary material available at https://doi.org/10.1038/s41612-025-00934-z.

Correspondence and requests for materials should be addressed to Qishen Huang, Yun-Hong Zhang or Maofa Ge.